

# A Lattice Gas Model for Organic Mixed Conductors: The Charge Carrier Vapor–Liquid Transition

Lukas M. Bongartz

*Institute for Applied Physics, Technische Universität Dresden, Nöthnitzer Str. 61, 01187 Dresden, Germany*

(Dated: November 27, 2025)

Organic mixed conductors (OMCs) represent a promising class of materials for applications in bioelectronics, physical computing, and thermoelectrics. OMCs feature intricate dynamics spanning multiple length and time scales, involving coupling between electronic, ionic, and mass transport. These characteristics set them notably apart from traditional semiconductors and hinder the description by conventional semiconductor theory. In this Letter, we approach the charge carrier modulation of OMCs using statistical mechanics. We discuss OMCs from a first-principles perspective and contrast them with established semiconductor materials, highlighting key differences in their collective charge carrier dynamics. This motivates our toy model describing OMCs as a lattice gas, which we analyze within the grand canonical ensemble. The model exhibits a first-order phase transition analogous to a classical vapor–liquid transition, governed by temperature and chemical potential. In doing so, it naturally explains the formation of distinct low- and high-density carrier phases as reported in recent literature. It also demonstrates how metastability near the phase boundary can give rise to history-dependent characteristics in device operation. This work provides a simple motivation for applying statistical mechanics to describe OMC behavior, offering a more natural description than traditional models developed for materials of fundamentally distinct character.

## I. INTRODUCTION

Organic mixed conductors (OMCs) – semiconducting polymers that allow for both ion and electron transport – represent a novel class of electronic materials, distinct from conventional inorganic systems like silicon [1]. While traditional semiconductors are generally operated (switched between conductive and non-conductive states) using the field effect, OMCs are controlled electrochemically. In this mode, the dynamic introduction and retrieval of dopants into the semiconductor become a central part of device operation, as opposed to the singular introduction of dopants during fabrication in legacy systems.

While OMC technology is still in its infancy and fundamental research stage, it is beginning to crystallize as a promising candidate to complement application layers inaccessible to silicon et al. These include, in particular, bioelectronics such as neural interfaces and neuromorphic computing [2]. The archetypal OMC device is the organic electrochemical transistor (OECT) [3]. In this device architecture, the semiconductor channel is coupled to a gate electrode via an electrolyte. The electrolyte acts as an ion reservoir, donating dopants into the polymer semiconductor mesh, where they compensate the (n- or p-type) electronic charge carriers hosted within the OMC’s  $\pi$ -system. As in conventional transistor devices, source and drain contacts probe the channel conductivity in terms of a drain current, with the key difference that carriers are driven throughout the entire volume of the channel, rather than being confined to the surface. We want to stress that OMCs represent one of the most diverse materials classes developed to date, where minor modifications in the molecular structure or material processing can manifest in profound differences on the mi-

croscopic scale (e.g., morphology, carrier mobility, mass and charge capacity) [4]. In this Letter, we aim for a first-principles, holistic point of view on OMCs, abstracting from microscopic details to the general characteristics of charge carrier dynamics, and will thus refer to generalized model systems of both silicon-like and carbon-based polymer semiconductors. This viewpoint already allows us to identify several key distinctions between the physics governing these material classes:

Most notably, OMC operation features extremely high charge carrier densities ( $\approx 10^{20}$ – $10^{21} \text{ cm}^{-3}$ ), orders of magnitude beyond what is typical in inorganic systems and approaching a 1:1 population of electronic charges on the molecular hosting sites [5–7]. Due to the disordered morphology, charge transport is often of a hopping nature, rather than band-like [8–10]. As carbon-based systems, OMCs also feature low dielectric constants [11, 12]. This circumstance contributes to an amplification of charge carrier interactions, enhancing both Coulomb and higher-order multipole contributions. As we outline in a simple estimation in Appendix A, this suggests coupling strengths that exceed silicon-based systems by several  $k_B T$ , which holds across the entire regime of relevant electron densities ( $10^{16}$ – $10^{19} \text{ cm}^{-3}$  and  $10^{18}$ – $10^{21} \text{ cm}^{-3}$ , respectively). Evidently, this condition has meaningful implications for the charge carrier dynamics, underlying, among others, deviations from the standard Miller-Abrahams framework for hopping transport [13].

We here focus on the charge carrier density and its modulation by an external bias, while leaving the incorporation of transport phenomena for a follow-up publication. Several works have shown the impact of particle interactions in OMC operation, such as electron–electron [6, 14], electron–phonon [15], and electron–dopant modes [6, 16, 17]. Collectively, these give rise to a dynamic

density of states that evolves with the carrier density itself and contribute to a heterogeneous doping process. They reveal an intricate configurational landscape involving the coupling between electronic charge carriers, mobile ionic dopants, molecular vibrations, and morphology. Two recent reports on an established OMC serve as an illustrative case study: Wu et al. provided direct experimental evidence that an electrochemically doped OMC forms  $\sim 10$  nm domains of distinct electronic character, whose growth is consistent with Model-B-type coarsening [18, 19]. This non-equilibrium phase separation is tied to a strong coupling between carrier populations and structural rearrangements, linking it to Cahn-Hilliard-like dynamics at the mesoscale [20]. Using the same OMC with a strongly interacting electrolyte, Bongartz et al. demonstrated OECTs with persistent hysteresis on experimental timescales, thermodynamically ascribed to a phase separation into domains of high and low doping degree [21].

These observations converge on a common underlying theme: a non-uniform stabilization of charge carriers, which suggests a connection to our coupling estimates discussed earlier (Appendix A). In inorganic systems like silicon, the electronically ‘hard’ environment causes charge carriers to remain strongly delocalized, weakly interacting, and efficiently screened by fast electronic polarization, which suppresses correlation effects. This leads to the well-known description as a quasi-electron gas governed by effective-mass, nearly-free-carrier physics. This picture breaks down in electronically ‘soft’ materials such as polymer semiconductors, where slow and heterogeneous polarization modes lead to poor screening, enhanced polaron formation, and much stronger (quasi-)particle interactions. Here, the combination of strong carrier interactions and near-unity site occupation elevates configurational entropy to a central role in setting the carrier distribution. This situation is not captured in traditional semiconductor theory, which typically takes the quasi-electron-gas at its foundation.

In this Letter, we take seriously this perspective and use statistical mechanics to study the effect of carrier interactions, allowing us to reproduce several of the effects observed in OMCs. We treat the population of charge carriers using the grand canonical ensemble of a lattice gas, allowing us to shed light on collective and critical phenomena. Two driving forces, the energetic interactions between doped sites and configurational entropy, compete in controlling the degree of carrier aggregation. The emergence of phase-separated domains and hysteretic bistability can be understood in analogy to a collective vapor–liquid phase transition. We first review the lattice gas in terms of its microscopic states and interactions before formalizing the corresponding grand canonical probability distribution. We close by connecting this statistical picture to the experimental observables in transistor operation.

## II. MAIN

### A. The Lattice Gas Model

The intricate dynamics and disordered microstructure of OMCs give rise to a vast number of possible microscopic arrangements of charge carriers, known as microstates. Meanwhile, device operation typically probes macroscopic properties, such as the total channel conductivity or impedance, which represent ensemble averages over the microscopic landscape. This perspective motivates a statistical treatment to determine the system’s equilibrium properties. We focus on the subsystem that gives rise to the measurement output of drain current: localized electronic charge carriers that are strongly coupled to local lattice distortions. This subsystem can be effectively decoupled from the bulk material following a separation of timescales between mobile, charge-carrying entities and large-scale structural rearrangements. In that sense, we treat the molecular backbone as a quasi-static grid of sites that hosts the carrier population. This picture maps onto a lattice gas model, which is mathematically equivalent to the Ising model: each site can either be empty or occupied by a single unit, denoted by an occupation number  $n_i \in \{0, 1\}$ .

Charge carriers in soft, conjugated polymers are not free electrons but quasi-particles often referred to as polarons, where the electronic charge is strongly coupled to local, fast vibrations of the molecular lattice (strong electron–phonon coupling)[22]. Rather than being point-like, the electronic charge is here delocalized over several repeat units (along the backbone and across  $\pi$ – $\pi$  stacks), which reduces the Coulomb self-energy and can lead to sizable dipole moments and polarizability. In coupling to the lattice relaxation, it deepens the associated potential well and, for sufficiently strong electron–phonon coupling, can make it energetically favorable for a second polaronic carrier to occupy the same region. These cooperative, short-range effects can outweigh the residual like-charge repulsion, motivating our central assumption of a net effective attraction between charge carriers. This energetic stabilization is analogous, in spirit, to the attractive part of intermolecular potentials (e.g., Lennard-Jones) that drives the condensation of classical fluids from a vapor.

In operation, an OMC is not an isolated system; it is in contact with a thermal environment (the ‘heat bath’) and a reservoir of dopant ions (the electrolyte). By the separation of timescales, the number of molecular host sites constitutes a constant effective volume ( $V$ ) for the electronic subsystem. The exchange of energy with the heat bath is governed by the temperature ( $T$ ), while the exchange of particles (charge carriers) with the reservoir is governed by the chemical potential ( $\mu$ ). This perspective, allowing for particle exchange within a fixed effective volume, naturally leads to the grand canonical ensemble. For a microstate  $X$  with  $N(X) = \sum_i n_i$  carriers, the

probability follows the Boltzmann distribution:

$$\mathbb{P}[X] \propto \exp\left(-\frac{E(X) - \mu N(X)}{k_B T}\right) \quad (1)$$

where  $E(X)$  is the internal energy of the microstate and  $N(X) = \sum_i n_i$  is the total number of carriers. For simplicity, we set  $k_B = 1$  henceforth.  $E(X)$  is defined by the Hamiltonian for our lattice gas:

$$H[X] = -J_0 \sum_{\langle i,j \rangle} n_i n_j, \quad (2)$$

where  $J_0 > 0$  is the microscopic attractive interaction energy between nearest-neighbor carriers motivated previously. We interpret  $\mu$  as a fixed reservoir parameter (control parameter) and will later connect it to the electrochemical potential in device operation.

While the probability of a single microstate may be known, the probability of an observable macrostate (e.g., one with a specific carrier density  $\rho = N/V$ ) must also account for its degeneracy, that is, the total number of microstates,  $\Omega$ , that may realize it. The probability of such a macrostate is proportional to the Boltzmann factor weighted by this degeneracy:  $\mathbb{P}(\text{macrostate}) \propto \Omega \cdot e^{-(E-\mu N)/T}$ . This degeneracy is quantified by the configurational entropy,  $S = \ln \Omega$ . Substituting this into the probability expression reveals the central role of the thermodynamic potential:

$$\mathbb{P}(\text{macrostate}) \propto e^S e^{-(E-\mu N)/T} = e^{-\Phi/T} \quad (3)$$

where the grand potential is defined as  $\Phi = E - TS - \mu N = F - \mu N$ , with  $F = E - TS$  being the Helmholtz free energy. The system's equilibrium state is the one that maximizes this probability, i.e., which minimizes  $\Phi$ . This setup represents the fundamental thermodynamic balance between the energetic drive for organization (minimizing  $E$ ), the entropic drive for ‘chaos’ (maximizing  $S$ ), and the coupling to the particle reservoir ( $-\mu N$ ).

## B. Monte Carlo Simulation

We investigate this model's equilibrium behavior using Monte Carlo simulations based on Glauber dynamics with Metropolis acceptance [23]. The algorithm repeatedly attempts to change the state of a randomly selected lattice site. A proposed flip (e.g., creating a carrier at an empty site) results in a change in the system's energy and particle number,  $\Delta E$  and  $\Delta N$ . The move is accepted with probability  $P_{\text{accept}} = \min(1, e^{-(\Delta E - \mu \Delta N)/T})$ , which ensures that the simulation correctly samples the grand canonical distribution and converges to the system's equilibrium state at fixed  $\mu$  and  $T$ .

We run the simulation across a grid of parameters  $(T, \mu)$  and map the system's equilibrium behavior. The result is the phase diagram shown in Fig. 1, which plots the equilibrium charge carrier density  $\rho$  as a function of

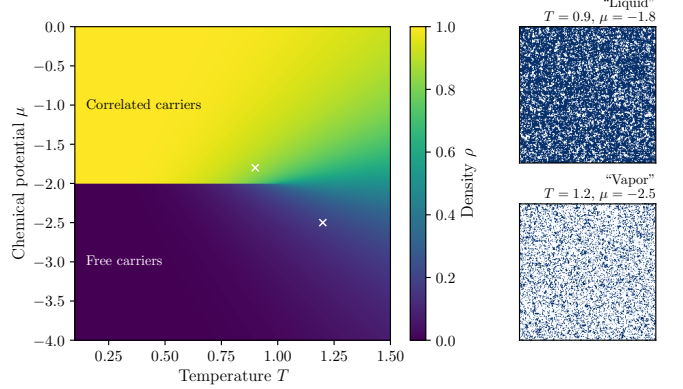


FIG. 1. Phase diagram of a lattice gas model, mapping equilibrium charge carrier density  $\rho$  against temperature  $T$  and chemical potential  $\mu$  ( $J = 1.0$ ). At high temperatures, density varies smoothly (supercritical fluid). At low temperatures, a sharp, first-order phase transition occurs at  $\mu_c = -2J$ , dividing a low-density “vapor” phase (free carriers) from a high-density “liquid” phase (correlated carriers). Insets show simulation snapshots for each phase.

temperature and chemical potential. The diagram reveals two distinct regimes. At high temperatures, the carrier density changes smoothly and continuously with  $\mu$ , analogous to a supercritical fluid. At low temperatures, a discontinuous jump appears in the density at a critical chemical potential  $\mu_c = -2J$  (Appendix B). This is a first-order phase transition, separating a low-density “vapor” phase of largely independent carriers from a high-density “liquid” phase of correlated, stabilized carriers. Near this phase transition line, the system exhibits metastability; if parameters are changed such that a new phase becomes favorable, the system can remain trapped in the previous macrostate for a very long time, as an energy barrier for nucleation of the new phase must be overcome. We provide a simulation tool under [24].

## C. Mean-Field Analysis

The regular square lattice in our simulation represents a significant idealization. Real OMCs are high-entropy materials whose long-chain polymers possess vast conformational degrees of freedom, resulting in substantial structural heterogeneity. While OMC microstructures can comprise mixtures of (semi-)crystalline and amorphous regions, a coarse-grained model can describe the collective system properties through the average interaction experienced by carriers, rather than through specific local geometric arrangements. To this end, we relax all geometrical constraints and adopt a mean-field approximation.

Here, every site is assumed to interact equally with every other site, creating a fully connected network. The interaction energy of a given state depends only on the total number of carriers,  $N(X)$ , not their specific arrange-

ment. For a system with  $V$  total sites, this leads to the coarse-grained interaction energy

$$E(X) = -\frac{2J}{V} N(X)^2, \quad (4)$$

where  $J$  is the effective mean-field coupling that encapsulates the underlying microscopic interactions (Appendix B). Substituting this expression into the grand canonical Boltzmann distribution gives

$$\mathbb{P}[X] \propto \exp\left(\frac{2J}{TV} N(X)^2 + \frac{\mu}{T} N(X)\right). \quad (5)$$

This formulation connects the probability of a single microstate to its macroscopic density  $\rho(X) = N(X)/V$ . To find the probability of observing a macrostate with a given density  $\rho$ , we must multiply by the number of ways to arrange  $N = \rho V$  carriers on  $V$  sites. This combinatorial factor gives rise to the system's entropy. A standard derivation using Stirling's approximation (Appendix C) allows us to write the probability distribution for the density  $\rho$  as

$$\mathbb{P}[\rho] \propto \exp\left(V\left[\frac{2J\rho^2 + \mu\rho}{T} - (\rho \ln \rho + (1-\rho) \ln(1-\rho))\right]\right), \quad (6)$$

For a large system ( $V \gg 1$ ), the probability distribution is sharply peaked around the density  $\rho^*$  that maximizes the term in the exponent. We can identify this exponent (per unit volume) as  $-\phi_{T,\mu}(\rho)/T$ , where  $\phi_{T,\mu}(\rho) = f(\rho) - \mu\rho$  is the mean-field grand potential density, with  $f(\rho) = -2J\rho^2 + T[\rho \ln \rho + (1-\rho) \ln(1-\rho)]$  being the Helmholtz free energy density. The relationship between the probability and the grand potential landscape is visualized in Fig. 2. The peaks in the probability distribution  $\mathbb{P}[\rho]$  correspond to minima in the grand potential density  $\phi_{T,\mu}(\rho)$ , which represent stable or metastable equilibrium states. At high temperatures ( $T > T_c$ ), the landscape features a single minimum that shifts continuously with  $\mu$ . Below the critical temperature, the landscape becomes non-convex and exhibits two minima. As the chemical potential crosses the critical value  $\mu_c$ , the global minimum of the grand potential jumps discontinuously from the low-density to the high-density state. This jump is the mathematical origin of the first-order phase transition.

#### D. Connection to Device Operation

In the lattice-gas description above, the charge carrier population is controlled by the chemical potential  $\mu$  that appears in the grand-canonical Boltzmann weight (Eq. (1)). In the mean-field analysis, this  $\mu$  enters Eq. (6) as an abstract control parameter that tilts the grand-potential landscape  $\phi_{T,\mu}(\rho)$  and thereby selects the most probable carrier density. Sweeping  $\mu$  along the  $\mu$ -axis of the phase diagram is equivalent to moving the system across the vapor–liquid phase boundary.

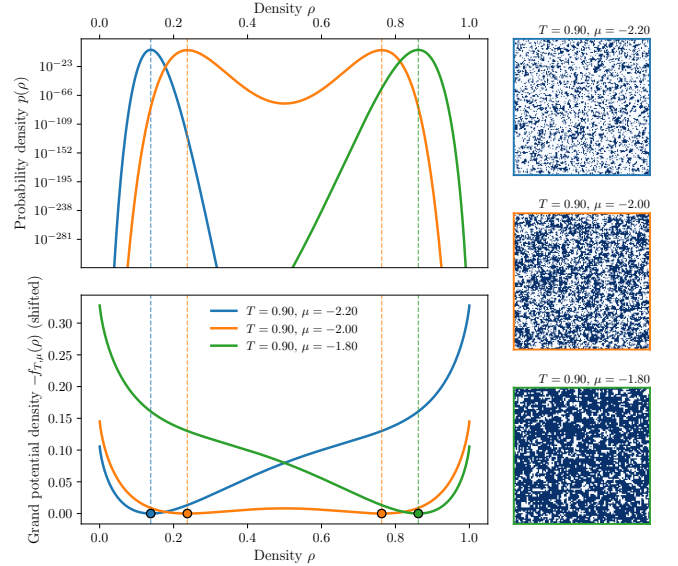


FIG. 2. Interplay of probability and grand potential in the mean-field model ( $J = 1.0$ ). (Top) Probability density  $p(\rho)$  as a function of carrier density  $\rho$ . (Bottom) The corresponding grand potential landscape,  $\phi_{T,\mu}(\rho)$  (shifted vertically for clarity). The peaks in probability correspond directly to the minima in the grand potential. As the chemical potential  $\mu$  increases, the most probable state (global minimum) shifts from a low-density “vapor” phase (blue) to a high-density “liquid” phase (green), passing through a coexistence point where both phases are equally probable (orange). Insets show representative simulation snapshots for each regime.

In device operation, this control parameter is set by the electrochemical environment provided by the electrolyte and gate. The electrolyte acts as a reservoir of ions that can exchange charge with the polymer channel, while the gate electrode controls the electrostatic potential of this reservoir relative to the channel. The electrochemical potential of a charge carrier of charge  $q$  is

$$\mu_{\text{ec}} = \mu_{\text{chem}} + q\phi, \quad (7)$$

where  $\mu_{\text{chem}}$  is the chemical contribution and  $\phi$  is the local electrostatic potential. The reservoir (electrolyte plus gate) is characterized by a fixed electrochemical potential  $\mu_{\text{reservoir}}$ . At equilibrium, the electrochemical potential in the channel must match that of the reservoir. Solving for the channel chemical potential that enters the lattice-gas weight gives

$$\mu_{\text{eff}} = \mu_{\text{reservoir}} - q\phi_{\text{ch}}. \quad (8)$$

Only a fraction of the applied gate voltage drops across the channel and couples to the hosting sites, which we capture by a coupling factor  $0 < \gamma \leq 1$ . At a local channel potential  $V_{\text{ch}}(x)$ , we approximate the electrostatic potential as  $\phi \approx \gamma(V_G - V_{\text{ch}})$ , so that the effective chemical potential entering the grand-canonical weight becomes

$$\mu_{\text{eff}}(V_G, V_{\text{ch}}) = \mu_{\text{reservoir}} - \gamma q(V_G - V_{\text{ch}}), \quad (9)$$

where  $\gamma = 1$  corresponds to ideal coupling and  $\gamma < 1$  accounts for partial screening and voltage division across gate, electrolyte, and channel. In the small-drain-bias limit where  $V_{\text{ch}} \approx 0$ , this reduces to the simpler form  $\mu_{\text{eff}} \approx \mu_{\text{reservoir}} - \gamma q V_G$ , making explicit that sweeping  $V_G$  is equivalent to sweeping the control parameter  $\mu$  in Eq. (6).

In the mean-field lattice gas, the occupation  $\rho$  of a site with local effective chemical potential  $\mu_{\text{eff}}$  obeys the self-consistency condition (derived in Appendix D)

$$\rho = \frac{1}{1 + \exp\left[-\frac{2J\rho + \mu_{\text{eff}}}{T}\right]}, \quad (10)$$

where  $J$  is the effective mean-field interaction strength and  $T$  is the dimensionless temperature. Combining Eqs. (9) and (10) gives the local occupation  $\rho(V_G, V_{\text{ch}})$  along the channel for a given gate and drain bias.

To connect this statistical picture to the drain current, we consider a one-dimensional channel of width  $W$ , thickness  $t$ , and length  $L$  biased by a drain voltage  $V_D$ . The drain voltage imposes a potential drop  $V_{\text{ch}}(x) \in [0, V_D]$  along the channel, so that  $\mu_{\text{eff}}$  and hence  $\rho$  become position dependent. Assuming drift-dominated transport with mobility  $\mu_{\text{tr}}$  and a density of available sites  $n_{\text{max}}$ , the local conductivity is

$$\sigma(V_G, V_{\text{ch}}) = q \mu_{\text{tr}} n_{\text{max}} \rho(V_G, V_{\text{ch}}). \quad (11)$$

In steady state, the drain current  $I_D$  is constant along the

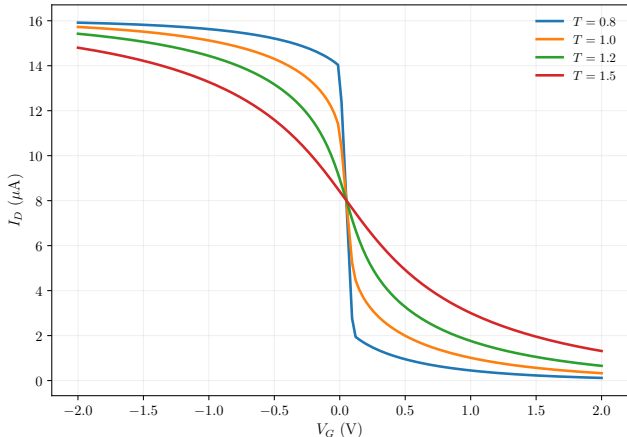


FIG. 3. Predicted transfer characteristics of an OECT from the interacting lattice-gas model. Shown is the drain current  $I_D$  as a function of gate voltage  $V_G$  at fixed drain bias  $V_D = 0.1$  V for several reduced temperatures  $T$ . Above the critical temperature, the response is smooth, whereas below, the first-order transition in carrier density produces an abrupt switching of  $I_D$  (only equilibrium branches are shown; long-lived metastable states would manifest experimentally as hysteresis). Currents are computed from Eq. (12) with  $J = 1.0$ ,  $\mu_{\text{reservoir}} = -2.0$ ,  $\gamma = 1.0$  and device parameters  $W = 50$  μm,  $L = 100$  μm,  $t = 100$  nm,  $n_{\text{max}} = 2 \times 10^{20}$  cm $^{-3}$ , and  $\mu_{\text{tr}} = 1$  cm $^2$ V $^{-1}$ s $^{-1}$ .

channel and obeys  $I_D = -\sigma(V_G, V_{\text{ch}}) W t dV_{\text{ch}}/dx$ . Eliminating the spatial coordinate  $x$  in favour of the channel potential  $V_{\text{ch}} \in [0, V_D]$  and integrating yields

$$I_D(V_G, V_D) = G_0 \int_0^{V_D} \rho(V_G, V_{\text{ch}}) dV_{\text{ch}}, \quad (12)$$

where

$$G_0 = \frac{q \mu_{\text{tr}} n_{\text{max}} W t}{L} \quad (13)$$

collects the geometric and kinetic prefactors (Appendix E). Together, Eqs. (6), (9), and (12) provide a link between the grand-canonical description and the measured drain current as a function of gate and drain bias. In the non-interacting limit ( $J = 0$ ), Eq. (12) reduces to a closed expression for  $I_D(V_G, V_D)$  obtained by analytic integration of the logistic occupation (Appendix F). In the small-drain limit,  $V_D \rightarrow 0$ , the channel potential is nearly uniform and  $\rho(V_G, V_{\text{ch}}) \approx \rho(V_G, 0)$ , so that Eq. (12) simplifies to

$$I_D(V_G, V_D) \simeq G_0 \rho(V_G, 0) V_D, \quad (14)$$

which is the regime illustrated in Fig. 3, where we plot the drain current  $I_D$  as a function of  $V_G$  at fixed  $V_D$ , assuming typical material and device parameters. Above the critical temperature, the response is smooth and reversible, whereas below, the first-order phase transition produces abrupt switching. In the presence of strong carrier–carrier coupling and slow nucleation dynamics, the system can remain trapped in metastable branches during a gate-voltage sweep, manifesting as a hysteresis between forward and backward traces.

The fundamental control parameter for the metastability is the ratio  $J/T$ , which encapsulates the balance between energetic and entropic contributions. This behavior reflects in experimental reports. For example, Ji et al. reported that OECTs treated with a hydrophobic agent exhibit an increased hysteresis width. In our framework, this treatment enhances coupling by repelling the aqueous solvent, thereby increasing the effective  $J$  [25]. Complementary to this, Bongartz et al. reported the inverse trend of shrinking hysteresis with rising temperature [21]. In general, these phenomena are characteristic of OECT systems engineered to be in a ‘strong-coupling’ regime, such as those employing ionic liquids and modified OMC composition, where the ratio  $J/T$  is significant.

### III. CONCLUSION

We have presented a minimal statistical-mechanics framework based on a lattice gas that describes the quasi-steady state of OMCs in the high charge density regime. Our results demonstrate that phenomena such as phase separation and hysteretic bistability can be understood in analogy to a collective vapor–liquid phase transition, driven by the competition between interaction energy

and configurational entropy. The direct connection between gate-voltage sweeps and trajectories through the thermodynamic phase diagram provides a natural explanation for the non-trivial transfer characteristics observed in devices operating in a strong-coupling regime. While this model is a strong simplification of the intricate molecular and electronic landscape of real OMCs, its ability to capture the essential features of a phase transi-

tion illustrates the principle of universality: near a critical point, the qualitative macroscopic behavior is governed chiefly by symmetries, dimensionality, and conservation laws rather than microscopic detail. This suggests that more refined descriptions, e.g., including transport phenomena, spatial heterogeneity, or diffusion, can be built on the same statistical-mechanical backbone, with  $J$  serving as a mesoscopic measure of correlation strength.

- 
- [1] B. D. Paulsen, K. Tybrandt, E. Stavrinidou, and J. Rivenay, Organic mixed ionic–electronic conductors, *Nature Materials* **19**, 13 (2020).
- [2] P. Gkoupidenis, Y. Zhang, H. Kleemann, H. Ling, F. Santoro, S. Fabiano, A. Salleo, and Y. Van De Burgt, Organic mixed conductors for bioinspired electronics, *Nature Reviews Materials* **9**, 134 (2024).
- [3] J. Rivenay, S. Inal, A. Salleo, R. M. Owens, M. Berggren, and G. G. Malliaras, Organic electrochemical transistors, *Nature Reviews Materials* **3**, 17086 (2018).
- [4] Y. Wang, S. Wustoni, J. Surgailis, Y. Zhong, A. Koklu, and S. Inal, Designing organic mixed conductors for electrochemical transistor applications, *Nature Reviews Materials* **9**, 249 (2024).
- [5] T. He and C. D. Frisbie, Sub-band filling, Mott-like transitions, and ion size effects in  $C_{60}$  single crystal electric double layer transistors, *ACS Nano* **16**, 4823 (2022).
- [6] D. H. L. Tjhe, X. Ren, I. E. Jacobs, G. D’Avino, T. B. E. Mustafa, T. G. Marsh, L. Zhang, Y. Fu, A. E. Mansour, A. Opitz, *et al.*, Non-equilibrium transport in polymer mixed ionic–electronic conductors at ultrahigh charge densities, *Nature Materials* **23**, 1712 (2024).
- [7] K. Xu, T.-P. Ruoko, M. Shokrani, D. Scheunemann, H. Abdalla, H. Sun, C.-Y. Yang, Y. Puttisong, N. B. Kolhe, J. S. M. Figueroa, *et al.*, On the origin of Seebeck coefficient inversion in highly doped conducting polymers, *Advanced Functional Materials* **32**, 2112276 (2022).
- [8] S. Fratini, M. Nikolka, A. Salleo, G. Schweicher, and H. Sirringhaus, Charge transport in high-mobility conjugated polymers and molecular semiconductors, *Nature Materials* **19**, 491 (2020).
- [9] S. Ihnatsenka, X. Crispin, and I. V. Zozoulenko, Understanding hopping transport and thermoelectric properties of conducting polymers, *Physical Review B* **92**, 035201 (2015).
- [10] G. Kim and K. P. Pipe, Thermoelectric model to characterize carrier transport in organic semiconductors, *Physical Review B* **86**, 085208 (2012).
- [11] R. Warren, P. W. M. Blom, and N. Koch, Molecular p-doping induced dielectric constant increase of polythiophene films determined by impedance spectroscopy, *Applied Physics Letters* **122**, 152108 (2023).
- [12] K. Ortstein, S. Hutsch, M. Hambach, K. Tvingstedt, B. Wegner, J. Benduhn, J. Kublitski, M. Schwarze, S. Schellhammer, F. Talnack, *et al.*, Band gap engineering in blended organic semiconductor films based on dielectric interactions, *Nature Materials* **20**, 1407 (2021).
- [13] N. Vukmirović and L.-W. Wang, Carrier hopping in disordered semiconducting polymers: How accurate is the Miller–Abrahams model?, *Applied Physics Letters* **97**, 043305 (2010).
- [14] M. Koopmans and L. J. A. Koster, Carrier–carrier Coulomb interactions reduce power factor in organic thermoelectrics, *Applied Physics Letters* **119**, 143301 (2021).
- [15] F. C. Spano and C. Silva, H- and J-aggregate behavior in polymeric semiconductors, *Annual Review of Physical Chemistry* **65**, 477 (2014).
- [16] M. Koopmans, M. A. T. Leiviskä, J. Liu, J. Dong, L. Qiu, J. C. Hummelen, G. Portale, M. C. Heiber, and L. J. A. Koster, Electrical conductivity of doped organic semiconductors limited by carrier–carrier interactions, *ACS Applied Materials & Interfaces* **12**, 56222 (2020).
- [17] L. M. Bongartz, G. LeCroy, T. J. Quill, N. Siemons, G. Dijk, A. Marks, C. Cheng, H. Kleemann, K. Leo, and A. Salleo, Electron–ion coupling breaks energy symmetry in bistable organic electrochemical transistors, *Communications Materials* **6**, 241 (2025).
- [18] R. Wu, D. Meli, J. Strzalka, S. Narayanan, Q. Zhang, B. D. Paulsen, J. Rivenay, and C. J. Takacs, Bridging length scales in organic mixed ionic–electronic conductors through internal strain and mesoscale dynamics, *Nature Materials* **23**, 648 (2024).
- [19] P. C. Hohenberg and B. I. Halperin, Theory of dynamic critical phenomena, *Reviews of Modern Physics* **49**, 435 (1977).
- [20] J. W. Cahn and J. E. Hilliard, Free energy of a nonuniform system. I. Interfacial free energy, *The Journal of Chemical Physics* **28**, 258 (1958).
- [21] L. M. Bongartz, R. Kantelberg, T. Meier, R. Hoffmann, C. Matthus, A. Weissbach, M. Cucchi, H. Kleemann, and K. Leo, Bistable organic electrochemical transistors: enthalpy vs. entropy, *Nature Communications* **15**, 6819 (2024).
- [22] R. Ghosh and F. C. Spano, Excitons and polarons in organic materials, *Accounts of Chemical Research* **53**, 2201 (2020).
- [23] N. Metropolis, A. W. Rosenbluth, M. N. Rosenbluth, A. H. Teller, and E. Teller, Equation of state calculations by fast computing machines, *The Journal of Chemical Physics* **21**, 1087 (1953).
- [24] L. M. Bongartz, An interactive lattice gas simulation tool, <https://lukasbongartz.github.io/rust-lattice-simulator/web-deploy/> (2025).
- [25] X. Ji, B. D. Paulsen, G. K. K. Chik, R. Wu, Y. Yin, P. K. L. Chan, and J. Rivenay, Mimicking associative learning using an ion-trapping non-volatile synaptic organic electrochemical transistor, *Nature Communications* **12**, 2480 (2021).

## Appendix A: Estimate of correlation energies

We perform a simple estimate of the charge carrier interaction energies in established (inorganic) and carbon-based polymer semiconductors. We consider the systems in terms of their three-dimensional charge carrier density  $n$  and relative permittivity  $\epsilon_r$ . Let the average carrier spacing follow with

$$r \approx n^{-\frac{1}{3}}. \quad (\text{A1})$$

Considering only the Coulomb energy  $E_C$  between two carriers, we define the dimensionless coupling strength as

$$\Gamma \equiv \frac{E_C}{k_B T}, \quad \text{with} \quad E_C = \frac{e^2}{4\pi\epsilon_0\epsilon_r} \cdot \frac{1}{r}. \quad (\text{A2})$$

Silicon devices typically feature carrier densities of  $n^{\text{Si}} \sim 10^{16}-10^{19} \text{ cm}^{-3}$  (moderate to high doping) with  $\epsilon_r^{\text{Si}} \approx 12$ . OMCs, on the other hand, are operated in the range of  $n^{\text{poly}} \sim 10^{18}-10^{21} \text{ cm}^{-3}$  with a permittivity of  $\epsilon_r^{\text{poly}} \approx 3$  for the ‘dry’ polymer backbone, where electronic carriers reside. While OMCs often incorporate screening electrolyte and solvent molecules in its pores, we note that local interactions within the molecular stack are still mostly governed by a low-dielectric environment. We compare the coupling strengths for these two systems in Tab. I. As a consequence of the high carrier density in combination with the low dielectric environment, this calculation suggests a carrier coupling that is significantly stronger in organic polymer semiconductors than in silicon systems. This conclusion even holds under a strong screening correction with  $\epsilon_r^{\text{poly}} \approx 10$ . Note that in this simple picture, restricting the silicon system to its sheet density in a 2D inversion layer hardly changes the estimated energies, since carrier spacing remains essentially the same.

TABLE I. Estimate of charge carrier interactions in silicon and polymer semiconductors.

$n [\text{cm}^{-3}]$	$r [\text{nm}]$	$E_C [\text{eV}]$	$\Gamma (T = 300 \text{ K})$
Si ( $\epsilon_r^{\text{Si}} \approx 12$ )			
$10^{16}$	46.4	0.003	0.1
$10^{18}$	10.0	0.012	0.5
$10^{19}$	4.6	0.026	1.0
Polymer ( $\epsilon_r^{\text{poly}} \approx 3$ )			
$10^{18}$	10.0	0.048	1.9
$10^{20}$	2.2	0.223	8.6
$10^{21}$	1.0	0.480	18.5
Polymer (‘wet’, $\epsilon_r^{\text{poly}} \approx 10$ )			
$10^{18}$	10.0	0.014	0.5
$10^{20}$	2.2	0.067	2.6
$10^{21}$	1.0	0.144	5.6

## Appendix B: Mean-field interaction and coexistence chemical potential

### 1. Mean-field interaction energy

Starting from the lattice-gas Hamiltonian of the main text,

$$H[X] = -J_0 \sum_{\langle i,j \rangle} n_i n_j, \quad (\text{B1})$$

we approximate the interaction energy in terms of the total number of occupied sites  $N(X) = \sum_i n_i$ .

In the mean-field picture every site is taken to see the average occupation  $\rho = N/V$  of all other sites, so that the interaction term for a given site  $i$  is approximated as

$$-J_0 \sum_{j \in \text{n.n.}(i)} n_i n_j \approx -J_0 z \rho n_i, \quad (\text{B2})$$

where  $z$  is the coordination number. Summing over all sites gives

$$E(X) \approx -J_0 z \rho \sum_i n_i \quad (\text{B3})$$

$$= -J_0 z \frac{N(X)}{V} N(X) \quad (\text{B4})$$

$$= -\frac{J_0 z}{V} N(X)^2. \quad (\text{B5})$$

It is convenient to define a coarse-grained mean-field coupling

$$J \equiv \frac{z}{2} J_0, \quad (\text{B6})$$

so that the interaction energy can be written as

$$E(X) = -\frac{2J}{V} N(X)^2. \quad (\text{B7})$$

Inserting this expression into the grand-canonical weight  $\mathbb{P}[X] \propto \exp[-(E(X) - \mu N(X))/T]$  used in the main text then yields

$$\mathbb{P}[X] \propto \exp \left[ \frac{2J}{TV} N(X)^2 + \frac{\mu}{T} N(X) \right]. \quad (\text{B8})$$

### 2. Mean-field coexistence chemical potential

In this mean-field description, the grand-potential density at temperature  $T$  and chemical potential  $\mu$  can be written as

$$\phi_{T,\mu}(\rho) = -2J\rho^2 + T[\rho \ln \rho + (1-\rho) \ln(1-\rho)] - \mu\rho, \quad (\text{B9})$$

where  $\rho$  is the carrier density ( $0 < \rho < 1$ ) and  $J > 0$  is the effective mean-field attraction defined above.

The coexistence (“critical”) chemical potential  $\mu_c$  is obtained by exploiting the particle-hole symmetry of the

lattice gas. At coexistence, the low- and high-density phases are equally stable, which in mean field corresponds to a symmetry of the grand potential under  $\rho \leftrightarrow 1 - \rho$ :

$$\phi_{T,\mu_c}(\rho) = \phi_{T,\mu_c}(1 - \rho) \quad \text{for all } \rho. \quad (\text{B10})$$

We therefore consider the difference

$$\Delta\phi(\rho) = \phi_{T,\mu}(\rho) - \phi_{T,\mu}(1 - \rho). \quad (\text{B11})$$

Using Eq. (B9), we obtain

$$\begin{aligned} \Delta\phi(\rho) &= \left[ -2J\rho^2 - \mu\rho \right] - \left[ -2J(1 - \rho)^2 - \mu(1 - \rho) \right] \\ &= -2J\rho^2 + 2J(1 - 2\rho + \rho^2) - \mu\rho + \mu(1 - \rho) \\ &= 2J(1 - 2\rho) + \mu(1 - 2\rho) \\ &= (1 - 2\rho)(2J + \mu). \end{aligned} \quad (\text{B12})$$

The entropic contribution cancels in the difference because  $\rho \ln \rho + (1 - \rho) \ln(1 - \rho)$  is symmetric under  $\rho \leftrightarrow 1 - \rho$ . At coexistence, we require  $\Delta\phi(\rho) = 0$  for all  $\rho$ , which is only possible if the prefactor of  $(1 - 2\rho)$  vanishes. This yields the mean-field coexistence chemical potential

$$\mu_c = -2J. \quad (\text{B13})$$

### Appendix C: Derivation of the Mean-Field Entropy

We review the derivation of the entropy term used in the mean-field analysis, which appears in Eq. (6). The goal is to find an analytical expression for the configurational entropy  $S$  of a macrostate defined by a carrier density  $\rho$ .

The entropy arises from the number of ways,  $\Omega$ , to arrange  $N = \rho V$  indistinguishable charge carriers on a lattice of  $V$  distinguishable sites. This is a classic combinatorial problem, and the number of microstates is given by the binomial coefficient:

$$\Omega = \binom{V}{N} = \frac{V!}{N!(V - N)!} \quad (\text{C1})$$

The configurational entropy is the natural logarithm of this quantity:

$$S = \ln(\Omega) = \ln(V!) - \ln(N!) - \ln((V - N)!) \quad (\text{C2})$$

For a macroscopic system,  $V$ ,  $N$ , and  $(V - N)$  are all very large numbers, making the direct computation of the factorials impossible. We can use Stirling's approximation for the natural logarithm of a factorial, which for large  $n$  is given by:

$$\ln(n!) = n \ln(n) - n + O(\ln(n)) \quad (\text{C3})$$

where  $O(\ln(n))$  represents terms that grow on the order of  $\ln(n)$ . Applying this expression to each term in the

entropy equation yields:

$$\begin{aligned} S &\approx (V \ln V - V) - (N \ln N - N) \\ &\quad - ((V - N) \ln(V - N) - (V - N)) \\ &\quad + O(\ln V) - O(\ln N) - O(\ln(V - N)). \end{aligned} \quad (\text{C4})$$

The expression simplifies to:

$$S \approx V \ln V - N \ln N - (V - N) \ln(V - N) + O(\ln V) \quad (\text{C5})$$

where we have combined the logarithmic error terms, as they are all of the same order. We now express  $N$  in terms of the density, so  $N = \rho V$ .

$$S \approx V \ln V - (\rho V) \ln(\rho V) - (V - \rho V) \ln(V - \rho V) \quad (\text{C6})$$

$$+ O(\ln V) \quad (\text{C7})$$

$$\begin{aligned} S &\approx V \ln V - \rho V (\ln \rho + \ln V) \\ &\quad - (1 - \rho)V (\ln(1 - \rho) + \ln V) + O(\ln V) \end{aligned} \quad (\text{C8})$$

Expanding and grouping the terms involving  $\ln V$ :

$$\begin{aligned} S &\approx (V - \rho V - (1 - \rho)V) \ln V \\ &\quad - V(\rho \ln \rho + (1 - \rho) \ln(1 - \rho)) + O(\ln V) \end{aligned} \quad (\text{C9})$$

The prefactor for the leading  $\ln V$  term is  $V - \rho V - V + \rho V = 0$ . This leaves us with the final expression for the entropy:

$$S \approx -V(\rho \ln \rho + (1 - \rho) \ln(1 - \rho)) + O(\ln V) \quad (\text{C10})$$

In the exponent of Eq. (6), this entropy term is combined with the energy term, which scales linearly with  $V$ . In the thermodynamic limit ( $V \rightarrow \infty$ ), the  $O(\ln V)$  term becomes negligible compared to the leading  $O(V)$  terms. We can therefore safely neglect it to arrive at the entropy density,  $s = S/V$ :

$$s = \frac{S}{V} \approx -(\rho \ln \rho + (1 - \rho) \ln(1 - \rho)) \quad (\text{C11})$$

This is the standard expression for the entropy of mixing, which forms the entropic part of the mean-field free energy density in Eq. (6).

### Appendix D: Mean-field lattice gas and local occupation

In the mean-field lattice-gas description, a site can be either undoped ( $n = 0$ ) or doped ( $n = 1$ ). For a configuration  $X$  with  $N(X)$  doped sites, the coarse-grained interaction energy is approximated as

$$E(X) = -\frac{2J}{V} N(X)^2 - \mu_{\text{eff}} N(X), \quad (\text{D1})$$

where  $J > 0$  is the effective mean-field interaction,  $V$  is the total number of sites, and  $\mu_{\text{eff}}$  is the effective chemical potential.

Within mean field, each site feels the average occupation  $\rho = \langle n_i \rangle = N/V$  of all other sites. The effective single-site internal energy can then be written as

$$E_i(n_i) \approx -(2J\rho + \mu_{\text{eff}}) n_i, \quad (\text{D2})$$

so that the two possible energies are

$$E_i(0) = 0, \quad E_i(1) = -(2J\rho + \mu_{\text{eff}}). \quad (\text{D3})$$

The corresponding single-site grand-canonical partition function is

$$Z_{\text{site}} = \sum_{n_i=0,1} \exp\left[-\frac{E_i(n_i)}{T}\right] = 1 + \exp\left[\frac{2J\rho + \mu_{\text{eff}}}{T}\right], \quad (\text{D4})$$

and the average occupation  $\rho = \langle n_i \rangle$  is

$$\rho = \frac{1}{Z_{\text{site}}} \sum_{n_i=0,1} n_i \exp\left[-\frac{E_i(n_i)}{T}\right] = \frac{\exp\left[\frac{2J\rho + \mu_{\text{eff}}}{T}\right]}{1 + \exp\left[\frac{2J\rho + \mu_{\text{eff}}}{T}\right]}. \quad (\text{D5})$$

This can be written in the compact logistic form

$$\rho = \frac{1}{1 + \exp\left[-\frac{2J\rho + \mu_{\text{eff}}}{T}\right]}, \quad (\text{D6})$$

which is the self-consistency condition quoted in Eq. (10) of the main text. Together with the device coupling

$$\mu_{\text{eff}}(V_G, V_{\text{ch}}) = \mu_{\text{reservoir}} - \gamma q(V_G - V_{\text{ch}}), \quad (\text{D7})$$

this defines the local occupation  $\rho(V_G, V_{\text{ch}})$  along the channel.

## Appendix E: Drift transport and current continuity

We now derive the expression for the drain current. Consider a one-dimensional channel of width  $W$ , thickness  $t$ , and length  $L$ , with coordinate  $x$  measured from source ( $x = 0$ ) to drain ( $x = L$ ). The local channel potential is  $V_{\text{ch}}(x)$ , with boundary conditions  $V_{\text{ch}}(0) = 0$  and  $V_{\text{ch}}(L) = V_D$ . The local carrier density is

$$n(x) = n_{\text{max}} \rho(V_G, V_{\text{ch}}(x)), \quad (\text{E1})$$

where  $n_{\text{max}}$  is the density of available redox sites. Assuming drift-dominated transport with mobility  $\mu_{\text{tr}}$ , the local conductivity is

$$\sigma(x) = q \mu_{\text{tr}} n(x) = q \mu_{\text{tr}} n_{\text{max}} \rho(V_G, V_{\text{ch}}(x)). \quad (\text{E2})$$

The current density is  $j(x) = \sigma(x)E(x)$  with electric field  $E(x) = -dV_{\text{ch}}/dx$ . The total drain current  $I_D$  is constant along the channel and given by  $I_D = j(x)Wt$ , so that

$$I_D = -q \mu_{\text{tr}} n_{\text{max}} \rho(V_G, V_{\text{ch}}(x)) Wt \frac{dV_{\text{ch}}}{dx}. \quad (\text{E3})$$

Rearranging yields

$$\frac{dV_{\text{ch}}}{dx} = -\frac{I_D}{q \mu_{\text{tr}} n_{\text{max}} Wt} \frac{1}{\rho(V_G, V_{\text{ch}}(x))}. \quad (\text{E4})$$

Separating variables and integrating from source to drain,

$$\int_0^{V_D} \rho(V_G, V_{\text{ch}}) dV_{\text{ch}} = \frac{q \mu_{\text{tr}} n_{\text{max}} Wt}{L} I_D, \quad (\text{E5})$$

where we have changed integration variable from  $x$  to  $V_{\text{ch}}$  and used  $V_{\text{ch}}(0) = 0$  and  $V_{\text{ch}}(L) = V_D$ . This leads directly to

$$I_D(V_G, V_D) = G_0 \int_0^{V_D} \rho(V_G, V_{\text{ch}}) dV_{\text{ch}}, \quad (\text{E6})$$

with

$$G_0 = \frac{q \mu_{\text{tr}} n_{\text{max}} Wt}{L}, \quad (\text{E7})$$

as stated in Eq. (12) of the main text.

## Appendix F: Non-interacting and interacting limits

In the non-interacting limit ( $J = 0$ ), the mean-field self-consistency relation Eq. (D6) reduces to a simple logistic dependence of the occupation  $\rho$  on the effective chemical potential  $\mu_{\text{eff}}(V_G, V_{\text{ch}})$  defined in Eq. (D7). Inserting this non-interacting  $\rho(V_G, V_{\text{ch}})$  into the integral expression for the drain current, Eq. (E6), yields a closed-form expression for  $I_D(V_G, V_D)$ . For  $J > 0$ , Eq. (D6) becomes genuinely non-linear and can admit multiple solutions for  $\rho$  at fixed  $(T, \mu_{\text{eff}})$ . The corresponding grand-potential landscape  $\phi_{T,\mu}(\rho)$  develops multiple minima, reflecting the coexistence of low- and high-density phases and giving rise to metastability. In this interacting case,  $\rho(V_G, V_{\text{ch}})$  must be obtained self-consistently for each pair  $(V_G, V_{\text{ch}})$ , and the drain current  $I_D(V_G, V_D)$  in Eq. (E6) has to be evaluated numerically. This is the regime relevant for the phase-separated behavior discussed in the main text.